

The Importance of Neighborhood Scheme Selection in Agent-based Tumor Growth Modeling



Georgios Tzedakis, Eleftheria Tzamali, Kostas Marias and Vangelis Sakkalis

Computational BioMedicine Laboratory, Institute of Computer Science, Foundation for Research and Technology-Hellas, Heraklion, Greece.

Supplementary Issue: Computer Simulation, Visualization, and Image Processing of Cancer Data and Processes

ABSTRACT: Modeling tumor growth has proven a very challenging problem, mainly due to the fact that tumors are highly complex systems that involve dynamic interactions spanning multiple scales both in time and space. The desire to describe interactions in various scales has given rise to modeling approaches that use both continuous and discrete variables, known as hybrid approaches. This work refers to a hybrid model on a 2D square lattice focusing on cell movement dynamics as they play an important role in tumor morphology, invasion and metastasis and are considered as indicators for the stage of malignancy used for early prognosis and effective treatment. Considering various distributions of the microenvironment, we explore how Neumann vs. Moore neighborhood schemes affects tumor growth and morphology. The results indicate that the importance of neighborhood selection is critical under specific conditions that include i) increased haptotactic coefficient, ii) a rugged microenvironment and iii) ECM degradation.

KEYWORDS: hybrid simulation, medical computing, tumors, Moore neighborhood, von Neumann neighborhood, cellular automata, cancel modeling, hybrid tumor model, *in silico* experiment

SUPPLEMENT: Computer Simulation, Visualization, and Image Processing of Cancer Data and Processes

CITATION: Tzedakis et al. The Importance of Neighborhood Scheme Selection in Agent-based Tumor Growth Modeling. *Cancer Informatics* 2015:14(S4) 67–81 doi: 10.4137/CIN.S19343.

TYPE: Original Research

RECEIVED: February 05, 2015. **RESUBMITTED:** May 20, 2015. **ACCEPTED FOR PUBLICATION:** May 21, 2015.

ACADEMIC EDITOR: J.T. Efrid, Editor in Chief

PEER REVIEW: Ten peer reviewers contributed to the peer review report. Reviewers' reports totaled 1,740 words, excluding any confidential comments to the academic editor.

FUNDING: The authors acknowledge support by the European Commission under the 7th Framework Programme project Computational Horizons in Cancer and the BIOSYS research project, Action KRIPIS, project No MIS-448301 (2013SE01380036) that was funded by the General Secretariat for Research and Technology, Ministry of Education, Greece and the European Regional Development Fund (Sectoral Operational Programme: Competitiveness and Entrepreneurship, NSRF 2007-2013)/ European Commission. The authors confirm that the funder had no influence over the study design, content of the article, or selection of this journal.

COMPETING INTERESTS: Authors disclose no potential conflicts of interest.

CORRESPONDENCE: sakkalis@ics.forth.gr

COPYRIGHT: © the authors, publisher and licensee Libertas Academica Limited. This is an open-access article distributed under the terms of the Creative Commons CC-BY-NC 3.0 License.

Paper subject to independent expert blind peer review. All editorial decisions made by independent academic editor. Upon submission manuscript was subject to anti-plagiarism scanning. Prior to publication all authors have given signed confirmation of agreement to article publication and compliance with all applicable ethical and legal requirements, including the accuracy of author and contributor information, disclosure of competing interests and funding sources, compliance with ethical requirements relating to human and animal study participants, and compliance with any copyright requirements of third parties. This journal is a member of the Committee on Publication Ethics (COPE).

Published by Libertas Academica. Learn more about this journal.

Introduction

Tumors are highly complex, self-organized biological systems spanning multiple scales from the molecular to cell and further to tissue level. Tumors are characterized by their increased heterogeneity and their ability to dynamically interact and adapt to changes of the microenvironment. A tumor begins with a few cells that have gained the ability to proliferate uncontrollably. The extensive heterogeneity is reflected in both the genetic diversity of the tumor mass as well as in its complex microenvironment that accommodates molecules important for cellular growth, proliferation, and migration. The continuous interaction among the cancer subpopulations and the tumor microenvironment drives tumor progression and invasion.

Tumor invasion involves the ability of tumor cells to migrate and invade into the surrounding host tissue microenvironment. Tumor cells are embedded in a fibrous material known as extracellular matrix (ECM), which is composed of macromolecules including collagens, laminin, and fibronectin. The structure and composition of the ECM play a critical role in tumor invasion, morphology, and metastasis because it

affects cell adhesion and motility.^{1,2} The ECM is constantly remodeled as the tumor grows. For example, cancer-associated fibroblasts produce extracellular proteins affecting the synthesis of ECM. Collagen filaments are reorganized and cancer cells produce enzymes that can degrade some of the components of the ECM. As the tumor mass becomes invasive, peripheral cells start detaching from the tumor mass, the compactness of its surface is lost, and tumor morphology is determined by the dynamic interactions between cells and the heterogeneous ECM. Cell movement is a complex process that has not yet been understood fully.^{2–6} It requires the activation of the actin-based machinery within the cell, which produces forces transmitted through cell–matrix adhesions on the surface areas of the cell that are in direct contact with the ECM. Under this consideration, the heterogeneity of the matrix such as the stiffness of the fibers, the various pore sizes, and the orientations of structures such as blood vessels, muscle fiber, and ECM play a significant role in cell movement. In addition to their haptotactic movement, tumor cell migration can be driven by gradients of diffusible substances such as oxygen,

glucose, or other signals, a process known as chemotaxis. In order to facilitate their movement, tumor cells usually produce matrix-degrading enzymes (such as matrix metalloproteinases) that degrade the ECM locally.⁷ Furthermore, cancer cells can migrate either individually or collectively, increasing the complexity of migration dynamics.

The emergence of tumor invasion is fatal and numerous mathematical models and research work focus on understanding the underlying mechanisms with the ultimate aim to improve prognosis and therapeutic outcome.^{8–19} Mathematical models enable the exploration of multiple hypotheses that allow a better understanding of tumor evolution and its complex components, which cannot be easily tested in the laboratory. Furthermore, the models predict behaviors of the system that can either guide new targeted experiments or may be even used in clinical practice assuming a model is thoroughly validated. However, the complexity and diversity of the mechanisms that comprise tumor combined with its multi-dimensional nature make it a very challenging problem to model mathematically. Current mathematical models mostly focus on a single-scale modeling, the microscopic level that describes molecular interactions, the mesoscopic level that takes into account cellular interactions, or even the macroscopic level that describes tissue-level dynamics. Models that integrate various scales in their description are called multi-scaled. In terms of their mathematical basis, the models are either discrete cell-based or continuum models. The discrete modeling approaches, usually model cells as individual entities that follow a set of rules, which allow them to interact with their environment.^{9,16} In this case, space and time are of discrete nature. The rules determining cell's behavior are usually biologically or experimentally inspired. On the other hand, the continuum methods approximate cancer cells and their microenvironment as continuous concentrations described by partial differential equations.^{17,20,21} Cell-based models are probably more appropriate for studying tumor invasion, as its evolution involves the migration of a few cells.

Discrete cell-based models can be further subdivided into (i) on-lattice, cellular automata models, which assume that cells lie on a fixed lattice structure, and (ii) off-lattice models, which are closer to a real representation of cells, but they are more difficult to implement.²² Each tumor cell in the cellular automata model is usually represented by a single lattice site. The lattice structure can constrain the neighborhood on which cell–cell interactions occur. In square lattices, a cell can have either four (von Neumann neighborhood) or eight (Moore neighborhood) neighbors. Cellular automata models have been widely used to describe physical systems because of their strong advantage to remain simple, yet capable of producing rather complex behaviors.

In this work, we present a hybrid approach, based on a model initially proposed by Anderson.¹ Hybrid models address the multiscale nature of cancer complex phenomenon by combining both discrete and continuous variables. A rule-based

stochastic cellular automata model on a two-dimensional (2D) square lattice that describes cellular proliferation and movement at cell level is combined with a continuum deterministic model that describes the chemical/ECM dynamics of the microenvironment. We show how a simple extension from von Neumann to Moore neighborhood in cell migration can better approximate cellular motility by minimizing the artifacts arising from lattice anisotropies and how the neighborhood selection can significantly affect tumor growth and morphology under specific conditions.

Hybrid Model of Tumor Growth Description

The mathematical model utilized in this work consists of two interacting components, the discrete one reflecting the tumor cells and the continuous one representing the extracellular environment. The environmental component refers to the tumor microenvironment that includes the oxygen concentration and the ECM density. Both are modeled by continuous variables, whereas the tumor cells are modeled in a discrete way using cellular automata that move, proliferate, and die independently following a set of rules. We further assume that cells lie on a fixed square lattice structure and that each lattice site can accommodate only one tumor cell. Cells can move to a neighboring site that is not occupied by another cell. In cellular automata, the two most commonly used neighborhoods are the von Neumann and the Moore neighborhoods, which take into account the four and eight neighbors of a cell, as seen in Figure 1. The main focus of this work lies on the analysis of how different neighborhood schemes affect cell movement and eventually tumor evolution and morphology. Hence, the way cell movement is approached plays a vital role and will be analyzed in detail in the following section.

Continuum component. Oxygen. We assume that the tumor is fully and homogeneously vascularized, ie, nutrient sources exist in every grid point of the computational domain. For simplicity, we assume that, the basic nutrient needed by the tumor cells for their growth and proliferation is oxygen.¹ Oxygen is produced by the established vasculature and diffuses into the extracellular space. The equation that describes the spatiotemporal evolution of oxygen is the following:

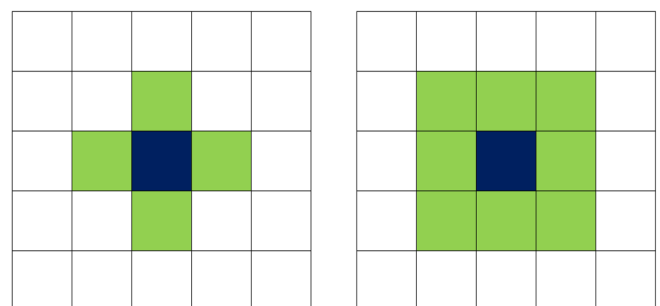


Figure 1. The cellular automaton neighborhoods von Neumann and Moore are visually represented on the left and right, respectively.

$$\frac{\partial o}{\partial t} = \nabla \cdot (D_o \nabla o) + \beta - b_o - \gamma c_{i,j} o \quad (1)$$

where $o(\mathbf{x}, t)$ represents the oxygen concentration and D_o, b, β, γ indicate the oxygen diffusion coefficient, the natural oxygen decay, the oxygen production by the sources, and its consumption by tumor cells, respectively. The term $c_{i,j} \in \{0, 1\}$ is provided by the discrete model part (discussed in the next section) and illustrates the absence or presence of a cancer cell on the grid point i, j . Consumption by healthy cells is assumed to be negligible.

It should be noted that real tumors are highly more heterogeneous than the above simplifications. Other components of the microenvironment that the continuous compartment could accommodate, such as glucose and hydrogen ions, also play a significant role in tumor.²³ On top of that, real tumor vessels are tortuous, dilated, and leaky; factors which considerably affect the homogeneity of nutrient supply and removal of waste products. However, considering that the focus of our model was to examine the tumor morphologies that arise from the discrete component and not from the interactions of cells with a complex microenvironment, we preferred to oversimplify the continuous component. Nevertheless, as a step toward more realistic cases, cellular migration on a random ECM has also been investigated.

Discrete component. Cell life cycle and proliferation. Each tumor cell is individually tracked. Each cell can live or die depending on the local oxygen concentration. A living cell can proliferate if it is mature and if there is available space for its daughters or else it becomes quiescent. The lifecycle of a tumor

cell is illustrated in the flowchart of Figure 2. Specifically, at each time step, the cell checks if the local oxygen level is under a certain threshold o_d . If that condition holds true, then the cell cannot continue living and dies. As soon as a cell dies, the space it was occupying is treated as vacant and can be filled by other cancer cells.

In this work, all tumor cells are assumed identical with respect to their phenotypic characteristics. Under this consideration, all cells proliferate at the same rate. Tumor cells with local oxygen concentration above o_d prepare for proliferation, increasing their age at each time step. We assume that the increment of the cellular age depends linearly on local resource availability such that limited oxygen results in smaller increments of the cellular proliferation age. Specifically, if the cell age is updated every t , the cell age is incremented by $o(i, j) \cdot t$, where $o(i, j)$ is the value of the normalized oxygen concentration available to the cell, for which value the inequality $0 \leq o(i, j) \leq 1$ is true.

When a cell reaches its proliferation age, then it is ready to produce two daughter cells. However, proliferation can only occur if there is an empty space in the Moore neighborhood of the cell in order to place its daughter cells. One daughter cell replaces the parent and the other is placed in a neighboring empty site. If no empty space is available, the cell enters the quiescent state. Cells in quiescent state are thus ready to proliferate but cannot do so due to space restriction. An active cell is considered a living cell that is not mature. Having reached their proliferation age, quiescent cells are considered mature and are assumed to consume half the oxygen compared to the active cells.¹ On the other hand, in the event that an empty space is found, the current cell resets its age and makes an exact copy of itself to the empty position. If during the proliferation, multiple empty spaces are found in the neighborhood, a random one is chosen. For simplicity, we assume that mutations do not occur during the proliferation process.

In order to avoid artifacts that would occur if all the cells reached their proliferation ages simultaneously, initial cell ages are randomly assigned to them. Additionally, at each iteration of the lifecycle execution, the cells are updated in a random order. This ensures that at each iteration every cell randomly receives a different priority in the update queue.

Cell movement. Cancer cell movement is described in this work by the discretized form of the following advection-diffusion equation²⁴:

$$\frac{\partial c}{\partial t} = \overbrace{D_c \nabla^2 c}^{\text{random movement}} - \overbrace{\chi \cdot (\nabla f)}^{\text{haptotaxis/chemotaxis}} \quad (2)$$

Equation 2 implies that cell motion is dominated by two processes. The first term corresponds to random motility (diffusion), whereas the second term describes the directed migratory response of cells to gradients of either fixed, nondiffusible molecules such as collagens and fibronectin or to unbound,

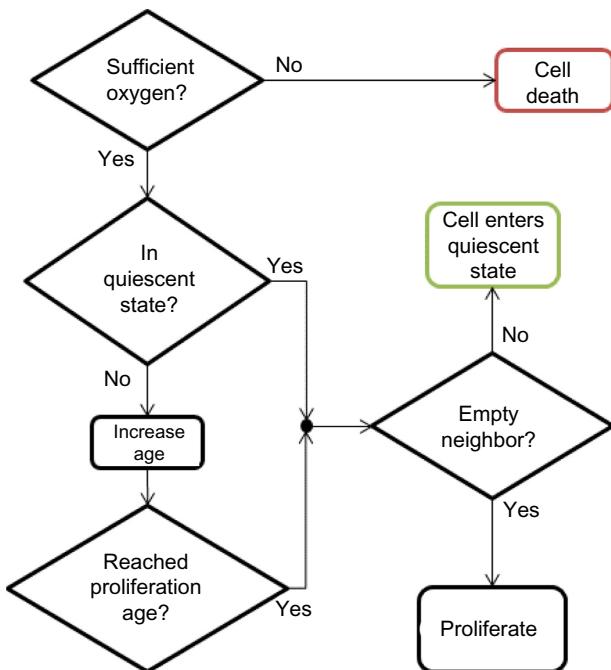


Figure 2. Cell life flow chart.



diffusible chemicals such as oxygen, processes known as haptotaxis and chemotaxis, respectively. The choice of the directed movement does not affect the form of the equation, but only changes the interpretation of the guided movement term, $\chi \cdot (\nabla f)$. It should be noted that if both chemotaxis and haptotaxis occur, a third term similar to the second term in Equation 2 can be easily added to describe the additive effect of these two processes.

The goal is to discretize movement and create rules that guide the cells in such a way that these discrete entities will behave like their continuous counterpart, namely, Equation 2.²⁵ In order to achieve that, standard finite-difference methods were used to numerically solve such equations. In the context of continuous variables, such methods utilize Taylor expansions to approximate the differentials of an equation, yielding a description of the shift of concentration from one grid point to its neighboring ones. The idea is that if small-enough space and time steps are used, the continuous solution can then be well approximated.

von Neumann neighborhood. The von Neumann neighborhood consists of upper, lower, left, right, and of course the central lattice points of the grid. It is the simplest 2D scheme on which finite differences can be applied. Equation 2 can be discretized using a standard five-point scheme following the von Neumann neighborhood that yields¹: $c_{i,j}^{k+1} = c_{i,j}^k P_0 + c_{i-1,j}^k P_1 + c_{i+1,j}^k P_2 + c_{i,j-1}^k P_3 + c_{i,j+1}^k P_4$, where the weights P_0, P_1, P_2, P_3, P_4 correspond to weights of concentration shifts as shown in Table 1.

Moore neighborhood. In finite differences, usually – but not necessarily – expansion of the neighborhood scheme increases the accuracy of the scheme as well as its computational load.^{26,27} We proceed by expanding the neighborhood to include the four diagonal points as well as the orthogonal ones. Likewise the nine-point finite-differences scheme can be used to yield weights to all nine points of a Moore neighborhood:

$$c_{i,j}^{k+1} = c_{i,j}^k P_0 + c_{i-1,j}^k P_1 + c_{i+1,j}^k P_2 + c_{i,j-1}^k P_3 + c_{i,j+1}^k P_4 + c_{i-1,j-1}^k P_5 + c_{i+1,j+1}^k P_6 + c_{i-1,j+1}^k P_7 + c_{i+1,j-1}^k P_8.$$

In short, we performed these calculations by approximating the first derivatives in two ways. The first approximation is the same as the one used in the von Neumann neighborhood and the second uses only the diagonal points. The latter approximation enables the computation of the weights to the extra four diagonal points. The final approximation for the derivative is defined as the average of the previous two. The corresponding weight values can be found in Table 2.

Choice of direction. Following the work of Anderson,¹ the probability that a cell will move toward a corresponding direction is proportional to the weight that describes the continuous concentration shift. To that purpose, the weights P_i are translated to ranges. The higher the weight value P_i , the longer the corresponding range R_i .

To construct the ranges R_i , at each time step, the weights P_i are calculated and normalized (dividing them by their sum) to obtain probabilities of motion. Then, five (or nine) probability ranges are computed

$$R_0 = (0, P_0), R_i = \left(\sum_{j=0}^{i-1} P_j, \sum_{j=0}^i P_j \right).$$

Finally, a random number r is generated between 0 and 1, and depending on the range in which this number belongs to, the tumor cell under consideration remains stationary if $r \in R_0$, moves left if $r \in R_1$, moves right if $r \in R_2$, moves down if $r \in R_3$, and moves up if $r \in R_4$. Additionally, exclusively for the Moore neighborhood moves diagonally right-down if $r \in R_5$, moves left-up if $r \in R_6$, moves right-up if $r \in R_7$, and moves left-down if $r \in R_8$.

If a cancer cell cannot move toward a certain region, such as in the case where the specific location is occupied by another cell, the weight P_i and the range R_i that lead toward that point are ignored. Furthermore, in case a weight is negative, then its absolute value contributes toward the opposite direction,

Table 1. Weights of concentrations shifts for the von Neumann neighborhood.

WEIGHT	CONCENTRATION SHIFT DESTINATION	VALUE
P_0	(i, j)	$1 - \frac{\delta_t}{h^2} (4D_c + \chi(f_{i-h,j} + f_{i+h,j} - 4f_{i,j} + f_{i,j-h} + f_{i,j+h}))$
P_1	$(i + 1, j)$	$\frac{\delta_t}{h^2} \left(D_c + \chi \frac{f_{i+h,j} - f_{i-h,j}}{4} \right)$
P_2	$(i - 1, j)$	$\frac{\delta_t}{h^2} \left(D_c - \chi \frac{f_{i+h,j} - f_{i-h,j}}{4} \right)$
P_3	$(i, j + 1)$	$\frac{\delta_t}{h^2} \left(D_c + \chi \frac{f_{i,j+h} - f_{i,j-h}}{4} \right)$
P_4	$(i, j - 1)$	$\frac{\delta_t}{h^2} \left(D_c - \chi \frac{f_{i,j+h} - f_{i,j-h}}{4} \right)$

Table 2. Weights of concentrations shifts for the Moore neighborhood.

WEIGHT	CONCENTRATION SHIFT DESTINATION	VALUE
P_0	(i, j)	$1 - \frac{\delta_t}{6h^2} (20D_c + \chi[4f_{i+h,j} + 4f_{i-h,j} - 20f_{i,j} + 4f_{i,j+h} + 4f_{i,j-h} + f_{i+h,j+h} + f_{i-h,j-h} + f_{i+h,j-h} + f_{i-h,j+h}])$
P_1	$(i + 1, j)$	$\frac{\delta_t}{24h^2} [16D_c + 3w_n \chi (2w_n f_{i+h,j} - 2w_n f_{i-h,j} + w_s f_{i+h,j+h} - w_s f_{i-h,j-h} + w_s f_{i+h,j-h} - w_s f_{i-h,j+h})]$
P_2	$(i - 1, j)$	$\frac{\delta_t}{24h^2} [16D_c - 3w_n \chi (2w_n f_{i+h,j} - 2w_n f_{i-h,j} + w_s f_{i+h,j+h} - w_s f_{i-h,j-h} + w_s f_{i+h,j-h} - w_s f_{i-h,j+h})]$
P_3	$(i, j + 1)$	$\frac{\delta_t}{24h^2} [16D_c + 3w_n \chi (2w_n f_{i,j+h} - 2w_n f_{i,j-h} + w_s f_{i+h,j+h} - w_s f_{i-h,j-h} - w_s f_{i+h,j-h} + w_s f_{i-h,j+h})]$
P_4	$(i, j - 1)$	$\frac{\delta_t}{24h^2} [16D_c - 3w_n \chi (2w_n f_{i,j+h} - 2w_n f_{i,j-h} + w_s f_{i+h,j+h} - w_s f_{i-h,j-h} - w_s f_{i+h,j-h} + w_s f_{i-h,j+h})]$
P_5	$(i + 1, j + 1)$	$\frac{\delta_t}{48h^2} [8D_c + 3w_s \chi (2w_n f_{i+h,j} - 2w_n f_{i-h,j} + w_s f_{i+h,j+h} - w_s f_{i-h,j-h} + w_s f_{i+h,j-h} - w_s f_{i-h,j+h} + 2w_n f_{i,j+h} - 2w_n f_{i,j-h} + w_s f_{i+h,j+h} - w_s f_{i-h,j-h} - w_s f_{i+h,j-h} + w_s f_{i-h,j+h})]$
P_6	$(i - 1, j - 1)$	$\frac{\delta_t}{48h^2} [8D_c + 3w_s \chi (-2w_n f_{i+h,j} + 2w_n f_{i-h,j} - w_s f_{i+h,j+h} + w_s f_{i-h,j-h} - w_s f_{i+h,j-h} + w_s f_{i-h,j+h} - 2w_n f_{i,j+h} + 2w_n f_{i,j-h} - w_s f_{i+h,j+h} + w_s f_{i-h,j-h} + w_s f_{i+h,j-h} - w_s f_{i-h,j+h})]$
P_7	$(i + 1, j - 1)$	$\frac{\delta_t}{48h^2} [8D_c + 3w_s \chi (2w_n f_{i+h,j} - 2w_n f_{i-h,j} + w_s f_{i+h,j+h} - w_s f_{i-h,j-h} + w_s f_{i+h,j-h} - w_s f_{i-h,j+h} - 2w_n f_{i,j+h} + 2w_n f_{i,j-h} - w_s f_{i+h,j+h} + w_s f_{i-h,j-h} + w_s f_{i+h,j-h} - w_s f_{i-h,j+h})]$
P_8	$(i - 1, j + 1)$	$\frac{\delta_t}{48h^2} [8D_c + 3w_s \chi (-2w_n f_{i+h,j} + 2w_n f_{i-h,j} - w_s f_{i+h,j+h} + w_s f_{i-h,j-h} - w_s f_{i+h,j-h} + w_s f_{i-h,j+h} + 2w_n f_{i,j+h} - 2w_n f_{i,j-h} + w_s f_{i+h,j+h} - w_s f_{i-h,j-h} - w_s f_{i+h,j-h} + w_s f_{i-h,j+h})]$

meaning that cells are attracted by the positive gradients and repelled by the negative gradients.

Directed movement scenarios. As discussed previously, cell movement is a complicated process and can have various driving mechanisms. Cells can move toward diffusible or nondiffusible chemicals and can migrate either individually or collectively depending on the absence or presence of cell–cell junctions. Furthermore, the structure and composition of ECM considerably affect cellular movement. In our work, we investigate some simplified scenarios of chemotaxis and haptotaxis in order to demonstrate the effect a neighborhood selection may have in tumor growth and morphology under specific conditions.

The first set of experiments assumes that the directed cell movement is driven exclusively by chemotaxis where the chemical attractor is assumed to be the oxygen concentration. This means that tumor cells prefer to move to sites of higher oxygen concentration. This set of experiments was constructed in order to take advantage of the oxygen distribution, which produces a dynamic gradient of radial symmetry and forms a tumor that it is expected to approximate a circular shape.

The second set of experiments considers the haptotactic movement of tumor cells, where cells are assumed to move up to gradients of macromolecules of the ECM, f . Although

it is reasonable to assume haptotaxis as one of the migration mechanisms followed by tumor cells, it should be noted that whether tumor cells move to denser areas of the ECM *in vivo* still remains an open question. The distribution of ECM is assumed random. As proposed in the work of Anderson,¹ a random distribution might be a more realistic representation of the highly heterogeneous ECM, while it allows the formations of invasive patterns under specific conditions. Furthermore, tumor cells usually remodel the ECM in order to further facilitate their movement. They produce matrix-degrading enzymes (such as matrix metalloproteinases) that degrade the ECM locally.⁷ In this work, we assume that tumor cells degrade the ECM locally when they are ready to move such that $f_{i,j} = 0$ and that immediately after the cell leaves the lattice site the ECM is reset to its previous condition. This implies that the ECM is quickly remodeled so that the movement of a cell does not leave any trace behind it to facilitate the movement of the other cells. Thus, cells migrate in an independent fashion making the emergence of invasion more difficult to occur. However, it should be noted that certain tumor types, like glioblastoma multiforme, have been observed to form invasive cell chains following paths of least resistance at least in *in vitro* experiments.²⁸

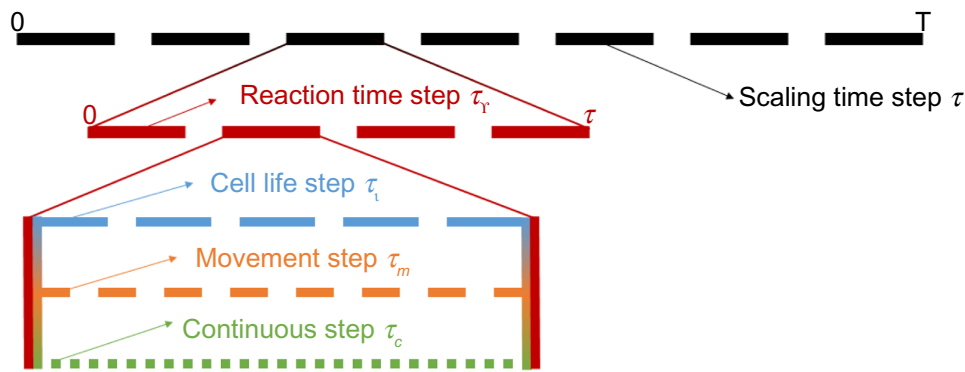


Figure 3. Visual representation of the time steps. See text for details.

Time steps. In order to perform nondimensionalization, the duration of iteration is chosen and is represented by τ . The total simulation time $[0, T]$ is segmented in pieces of τ length, each representing a single iteration of the model. Furthermore, each iteration time step is segmented in smaller steps noted as reaction time steps τ_r .

Reaction time step. The reaction step is assumed to be small enough for the model to be in a quasi-steady state. In essence, the running model compartment considers the variables controlled by the other model parts stable. From the perspective of a cell, for example, this means that during a reaction step the cell can follow its life cycle (ages, proliferates, and dies), while the state of the environment and the position of the cells are stationary. The respective principle is followed when calculating the next environment concentrations and cell positions.

Compartmental time steps. In addition to the τ_r time step, each modeling compartment operates at its own independent time step as illustrated in Figure 3. In particular, the continuous step τ_c is dictated by the method used to numerically solve the differential equation(s) that describe the microenvironment. Thus, in our case the continuous time step $t_c = \frac{h}{5}$ depends on the spatial step. The grid is forced to be very fine because as mentioned earlier each lattice point represents a cell, in turn requiring a small time step for the numerical solution. One could be tempted to choose the cell life and movement compartmental time steps equal to the continuous one; however, that would greatly impede the performance of the model.

As implied by the quasi-steady-state assumption, the environment and the cell positions remain unaffected while the life cycle updates the cell states. Therefore, the cell life flow chart in Figure 2 will always yield the same result. To

avoid unnecessary calculations, the cell life step τ_l can be set equal to the reaction step τ_r .

The choice of the movement time step τ_m dictates how many times a cell will calculate the movement probabilities per reaction time τ_r . We set as $k = \frac{\tau_r}{\tau_m}$ the number of possible movement attempts per reaction. For convenience, the movement time step is forced to be divisible by the reaction time step resulting in k being a natural number: $k \in \mathbb{N}$. To ensure that the finite-differences scheme used to retrieve the movement probabilities is valid, it is necessary that the value of P_0 is positive. Substitution of $\tau_m = \frac{\tau_r}{k}$ for $P_0 > 0$ results in two different values for k depending on the neighborhood scheme chosen (k_{VN} for von Neumann neighborhood and k_{Mo} for Moore neighborhood). Their corresponding values are shown in Table 3. It is noteworthy that the movement time step depends on both the diffusion coefficient D_c and chemotactic/haptotactic coefficient χ . In our experiments, both neighborhoods are investigated and thus k is chosen to satisfy both inequalities: $k = \min\{k_{VN}, k_{Mo}\}$.

Boundary conditions. When solving the Equation 1, which describes the oxygen, Dirichlet boundary conditions are preferred over no-flux (Neumann) boundary conditions. It is assumed that the surrounding domain is well vascularized, and thus the boundary oxygen is set to its maximum value of 1. It has been shown that this choice of boundary conditions results in computations that can approximate results as if the experiment was performed in a larger domain with no-flux boundary conditions, as long as the well-vascularized assumption holds true.²⁹

Simulation process and simplifications. In order to focus our study on cellular movement and the effect of neighborhood schemes on tumor growth and morphology, many simplifications have been made.

- i. Concerning the discrete part, a single phenotypic scheme was chosen to ensure that the movement and proliferation parameters are the same for all the populations. Furthermore, the cell-cell adhesion forces were ignored at this stage as we focus only on an expansion of the movement neighborhood.

Table 3. Choice of movements per reaction, k , for the two neighborhood cases.

VON NEUMANN	MOORE
$k_{VN} > \frac{4(D_c + \chi)}{h^2} \tau_r$	$k_{Mo} > \frac{10(D_c + \chi)}{3h^2} \tau_r$

Table 4. Parameter values.

SYMBOL	DESCRIPTION	VALUES
L	Domain size	1 cm
h	Spatial step	25 μm
N	Grid size	400
τ	Iteration time step	16 hours
D_o	Oxygen diffusion parameter	$10^{-5} \text{ cm}^2 \text{ s}^{-1}$
β	Oxygen production rate	0.25 (non-dimensional)
γ	Cancer cell Oxygen uptake	$25 \cdot 10^{-7} \text{ M cells}^{-1} \text{ s}^{-1}$
α	Oxygen decay	0.0125 (non-dimensional)
o_d	Oxygen threshold	0.25 (non-dimensional)
D_c	Cancer cell diffusion coefficient	$10^{-10} \text{ cm}^2 \text{ s}^{-1}$

- ii. The continuous part of the model was also stripped to its essentials to minimize run time and avoid any possible direct or indirect source for differentiation in the results arising from the interaction between the continuous concentrations of the microenvironment and the movement selection schemes. However, in a different set of experiments, a random ECM has been applied as a step toward more complex environments. In all the experiments, the tumor is considered homogeneously vascularized and neoangiogenesis is not taken into account.

Implementation. The model was implemented using MATLAB, C, and openMP. The MATLAB platform was extensively used and served as the program backbone. It was utilized to code the discrete model, to visualize the data, as well as to extract the statistics presented. The solution of the continuous part of the model was implemented in C due to its computational time-demanding nature. Also, the openMP library was used to perform

the computations in parallel for additional speed up when using multicore CPUs.

Results and Discussion

The simulations were performed on a 2D regular grid of size $L \times L$, where $L = 1 \text{ cm}$. Table 4 shows the main parameters used in our model as well as the characteristic spatial (L) and temporal (τ) scales that are used in order to nondimensionalize our equations. The space step h was selected assuming that each site on the computational grid can be occupied by only one tumor cell and that the tumor cell diameter is approximately 25 μm . Additional parameter values can be found in Table 4.

The oxygen concentration was initially set to its maximum saturation value in the whole domain. A square of edge equal to 15 at the center of the grid was filled with tumor cells with probability equal to 0.7 for each point to be filled with a tumor cell. Thus, the initial cancer resides in a square on the center of the domain that is roughly 70% populated.

We investigate the effect of neighborhood selection on tumor evolution considering various distributions of the microenvironment.

- i) We first assume a dynamic radial gradient arising from the distribution of oxygen that considers cells moving chemotactically toward higher oxygen concentrations.
- ii) We then explore a random distribution of the ECM where cells are encouraged to move haptotactically to denser areas of the matrix.

In order to quantitatively describe the morphology of the simulated tumors, several commonly applied metrics for the characterization of tumor pattern formation were used. Specifically, the normalized radial variance was applied to the first (i) above-mentioned scenario of radial symmetry, while the radius of gyration (gyradius) and roughness

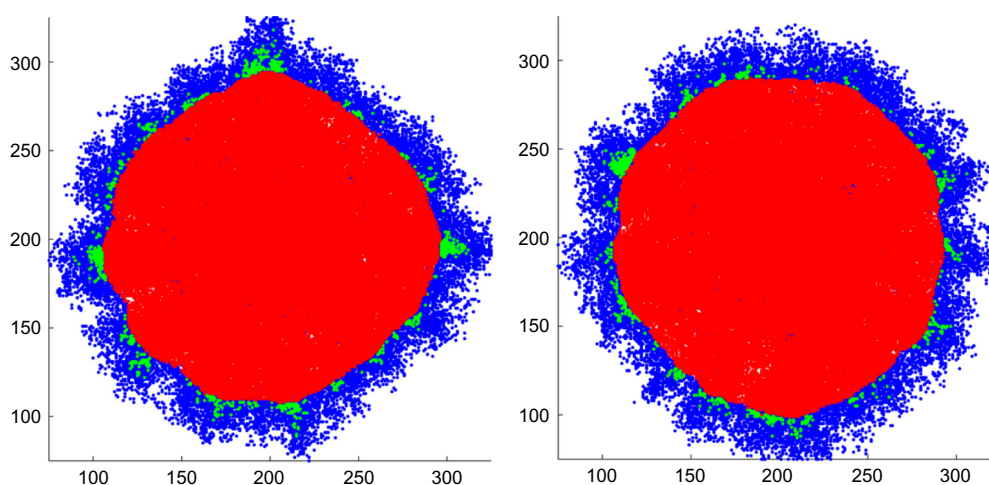


Figure 4. Results from the first set of 100 experiments, cancer cells after 100 iterations using the von Neumann and the Moore neighborhood at the left and the right column, respectively. The blue, green, and red cells denote living proliferative, living quiescent, and dead cancer cells, respectively.

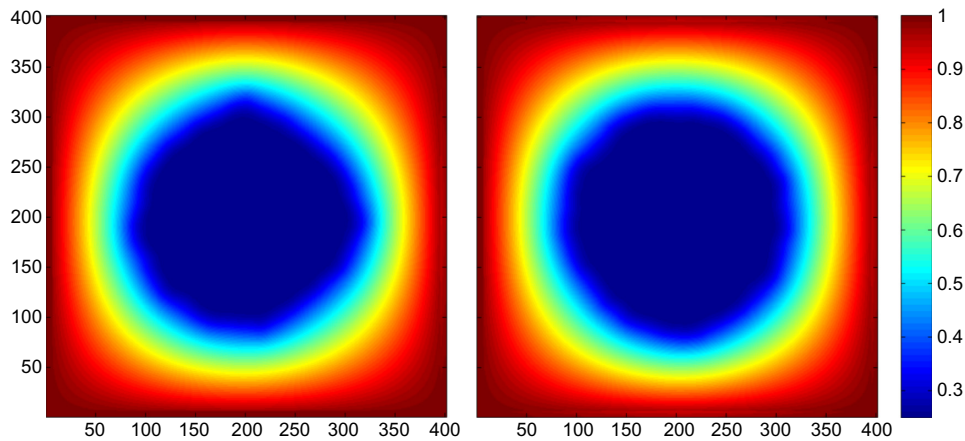


Figure 5. Results from the first set of 100 experiments, final Oxygen concentrations after 100 iterations using the von Neumann and the Moore neighborhood at the left and the right column, respectively.

metrics were used in the second scenario (ii) of random distributions.^{12,14,30}

Chemotactic movement to gradients of oxygen. In this set of experiments, it is assumed that cells move chemotactically directing their movement in response to oxygen concentration gradients. Taking into account the exact solution of Equation 2 under ideal circumstances (if the attractor consisted of round uniform radial gradients) and the fact that vascularization is homogeneous, the expected outcome is a round tumor.²⁴

In this scenario, cell positions are affected by oxygen gradients and oxygen concentrations are affected by cell positions. In practice, this adds a layer of interaction between the discrete and continuous components of the model. The parameters used in this set of experiments are as shown in Table 4. Furthermore, the proliferation time of tumor cells equals $A_p = 32$ h, the haptotactic coefficient is set to $\chi = 10^{-8} \text{ cm}^2 \text{ s}^{-1} \text{ M}^{-1}$, and the diffusion coefficient of the random movement equals $D_c = 10^{-11} \text{ cm}^2 \text{ s}^{-1}$.

To estimate the statistical significance of our results, 100 sets of experiments were executed. Random initializations were performed for the cancer cell population between the experiments as described in the previous subsection, while conserving the same initial state for each von Neumann and Moore set. The tumors were left to grow for 100 iterations, which corresponds to 1,600 fictitious hours (about 66.6 days).

The emerging tumor morphologies of the first set of experiments after 100 iterations can be seen in Figure 4 for the two different neighborhood schemes. Additionally, the growth of the tumor population over time can be seen in the two Supplementary chemotaxis videos, one for each neighborhood scheme. The corresponding oxygen distributions are also shown in Figure 5. The cells depicted with blue, green, and red color correspond, respectively, to proliferative, quiescent, and necrotic cancer cells. A proliferative rim of approximately 25 cells width is formed in both cases, while a few quiescent cells are sparsely distributed around the boundary that is

formed between the proliferative and necrotic cells. Due to the increased oxygen demands by tumor cells, necrosis covers most of the tumor at the end of the experiment.

In Figure 5, it can be seen that the selection of the neighborhood scheme affects the tumor morphology. In particular, the cells following the von Neumann scheme tend to form tumors of diamond shape, while the cells moving based on the Moore neighborhood form tumors that approximate a circular shape. Considering that the oxygen concentration is directly affected by the distribution of tumor cells (Equation 1), a similar pattern is also observed in the corresponding oxygen distributions as is shown in Figure 5. As expected, similar results are also produced when tumor cells are allowed to move chemotactically to a radially symmetric gradient similar

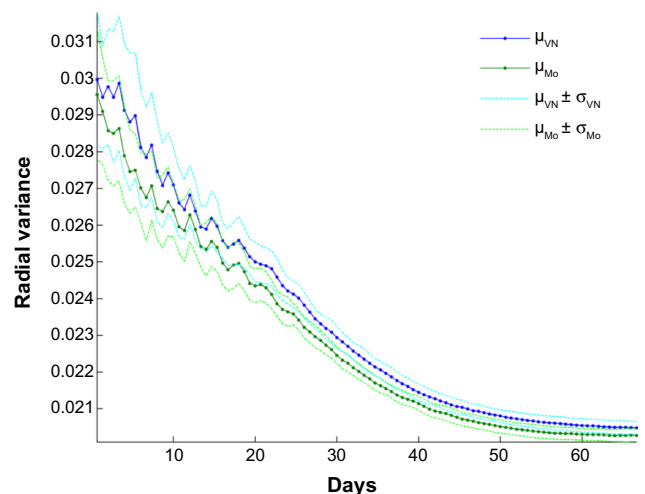


Figure 6. Mean normalized radial variance over time measured over the 100 sets of experiments for the two neighborhood schemes. The solid blue and green lines show the progression of the mean radial variance over time for the von Neumann and the Moore neighborhoods, respectively. The ranges created by the blue and green pairs of dashed lines contain the mean values if the radial variance plus and minus their standard deviations.

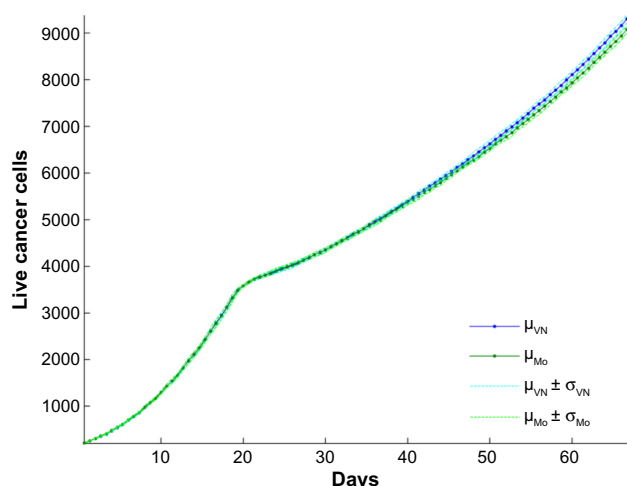


Figure 7. Number of live cells over time measured over the 100 sets of experiments for the two neighborhood schemes. The solid blue and green lines show the growth curves for the von Neumann and the Moore neighborhoods, respectively. The ranges created by the blue and green pairs of dashed lines contain the mean of the of live cancer cells plus and minus their standard deviations.

to the oxygen concentration but remains invariant over time (results in Section 1 of Supplementary Material).

To quantify the difference between the two neighbor selections, we define the radial variance metric as the variance of the distance of a tumor cell from the center and normalized it by dividing with the total number of the cells. For this metric, the dead cells were also included. The normalized radial variance is thus defined as:

$$d_{var} = \frac{1}{N^2} \sum_{i=1}^N (r_i - \bar{r})^2,$$

where r_i corresponds to the distance of the i -th cell from the center, N to the total number of cells at that time point, and \bar{r} to the mean value of the distances r_i . Among other shapes of the same size, circular discs have the smallest value of d_{var} . Figure 6 shows the mean values and the standard deviations of the normalized radial variance, d_{var} , for all the experiments over time. The Moore-based movement (depicted with green color in Fig. 6) shows consistently smaller value of the mean d_{var} than the corresponding von Neumann-based movement (depicted with blue color in Fig. 6). Figure 7 shows the mean number of live cells over time measured again over the 100 sets of experiments for the two neighborhood schemes. The standard deviations of the mean growth curves are depicted as well. Initially, the two curves coincide, however, after 45 fictitious days difference of the two population means reaches 260 cells.

In order to test the statistical significance of the differences, we first used D'Agostino–Pearson's K^2 test to verify the normality of each of our observations for every iteration

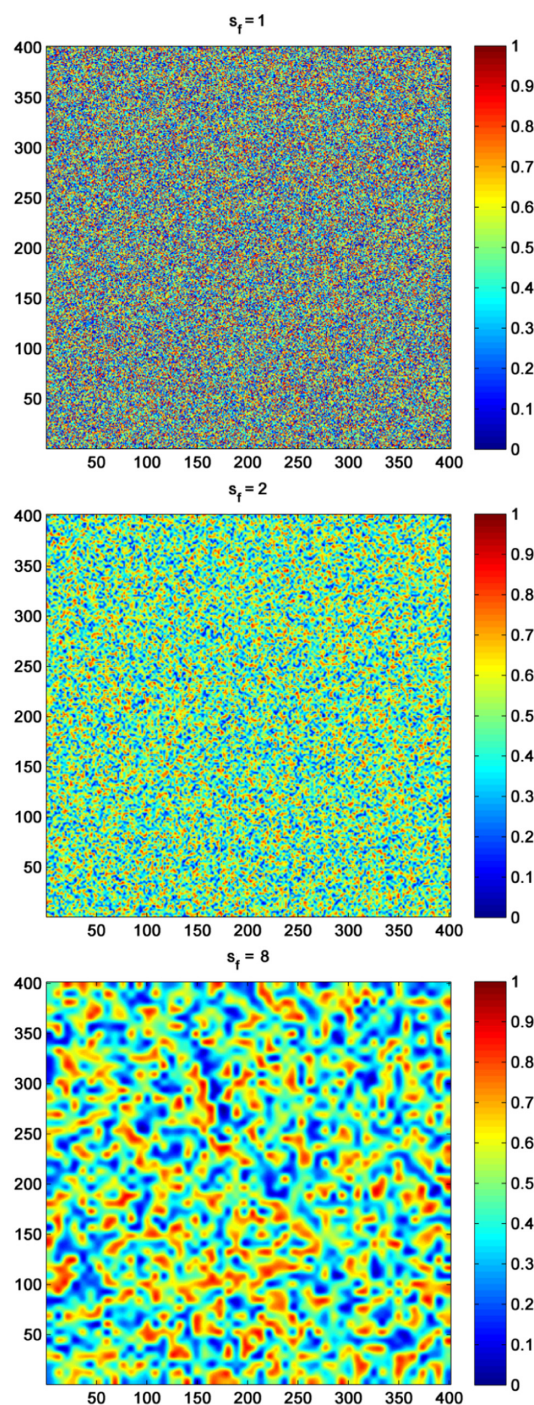


Figure 8. The random extracellular environments after being smoothed by varying smoothing factors. The top concentration contains no smoothing ($s_f = 1$), the one in the center was smoothed by $s_f = 2$ and the bottom by $s_f = 8$.

and movement scheme individually. Then t -tests for unequal variances were performed between the von Neumann and the Moore set of experiments for every iteration. Note that no multiple comparison adjustment was used. Both the live cells and the normalized radial variance metrics at the final time point produced p -values less than 10^{-6} , indicating statistically significant differences. It is noteworthy that

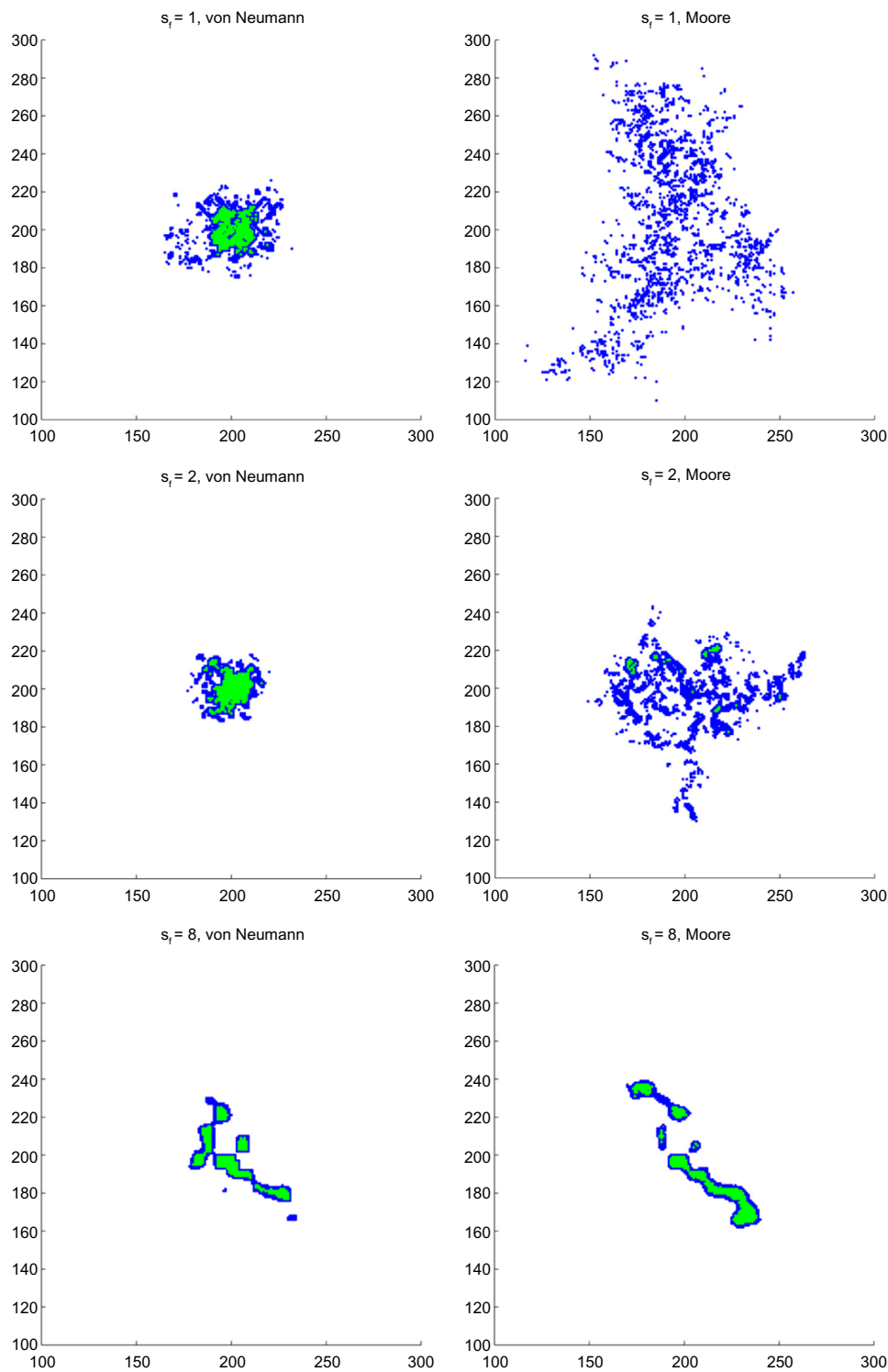


Figure 9. Final cancer cell distributions after 50 iterations. Blue cells are proliferating cancer cells and cells represented in green have entered the quiescent state. The von Neumann and the Moore results are shown in the left and the right columns, respectively. The first, second, and the third rows correspond to the various smoothing factor cases 1, 2, and 8.

the p -value of the radial variance drops below the threshold 0.05 earlier (3rd iteration) than the live cancer cells (59th iteration) hinting that the cause for the inconsistency of the sum of the live cells is the movement neighborhood.

Haptotactic movement to gradients of random ECM. To demonstrate the effect of neighborhood selection in haptotactic

movement, we assume that cells direct their movement in response to gradients of a random ECM. Various distributions of the ECM are considered as shown in Figure 8. In particular, the ECM distribution was created by drawing randomly pseudorandom values from the standard uniform distribution on the open interval (0,1) and smoothing the outcome

through bilinear interpolation by a factor $s_f = \{1, 2, 8\}$ and 8. To further facilitate their movement, we assume that tumor cells locally degrade the ECM when they move in a way such that $f_{i,j} = 0$ and that immediately after their movement the ECM is regenerated to its previous concentration.^{2,7} In this set of experiments, the haptotactic coefficient (χ) and the cellular proliferation time (A_p) take values $\chi = 4 \cdot 10^{-8} \text{ cm}^2 \text{ s}^{-1} \text{ M}^{-1}$ and $A_p = 16$ hours, respectively.

Figure 9 illustrates the emerging tumor morphologies for the different distributions of ECM and the two different neighborhood schemes after 50 iterations (800 simulation hours). Figure 9 demonstrates the importance of ECM distribution on tumor evolution. As can be seen (Fig. 9, columns), smoother ECM distributions produce more compact tumors. Furthermore, movement based on different neighborhood schemes also produces substantially different tumor morphologies. It appears that allowing cells to additionally move toward its diagonal points causes them to follow paths and reach locations that they would not be able to access otherwise. As the ECM becomes smoother (bottom row of Fig. 8), the emerging tumor morphologies for the different neighbors become more similar with each other (bottom row of Fig. 9) indicating that under the specific conditions the two approximations coincide.

To quantify the differences in spatial spread and invasive tumor morphology of the neighborhood schemes, the gyradius and the roughness metrics are introduced.^{12,14,30} The gyradius or radius of gyration is defined by:

$$R_g = \sqrt{N_c^{-1} \sum_{i=1}^{N_c} (r_i - r_{cm})^2},$$

where N_c, r_i , and r_{cm} are the total number of tumor cells, the distance of the i -th cell from the center of the domain, and the

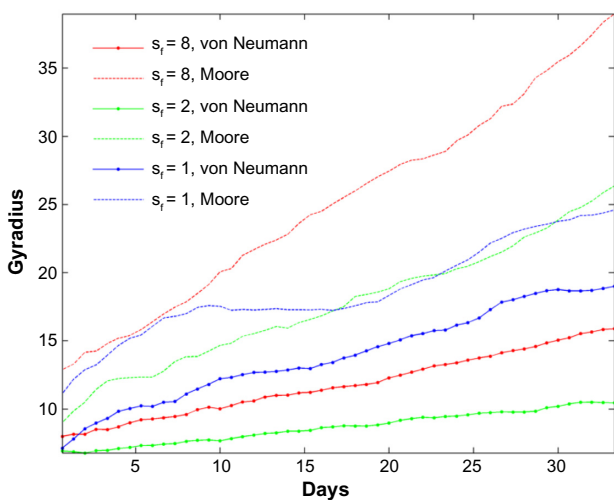


Figure 10. Gyradius metric over time. Blue, green, and red lines denote the $s_f = 1, 2,$ and 8 cases, respectively. The von Neumann cases are plotted with dotted lines and the Moore with dashed lines.

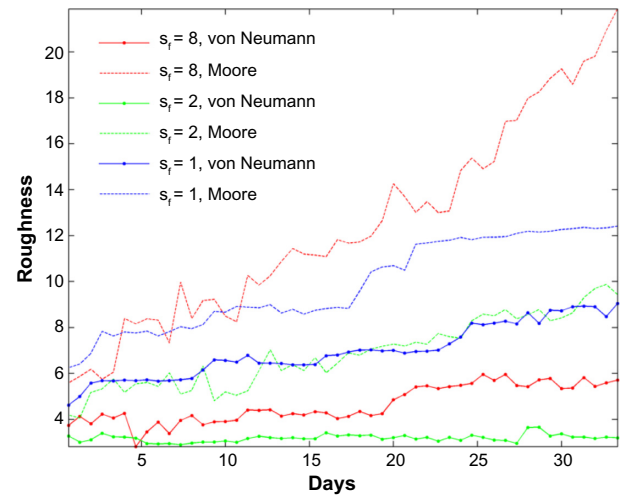


Figure 11. Roughness metric over time. Blue, green, and red lines denote the $s_f = 1, 2,$ and 8 cases, respectively. The von Neumann cases are plotted with dotted lines and the Moore with dashed lines.

distance of the center of mass from the center of the domain, respectively. The roughness is defined as:

$$R_{rough} = \frac{1}{N_{bin}} \sum_{i=1}^{N_{bin}} \|d_i - \langle d \rangle\|,$$

where N_{bin} is the number of bins made along the circumference of a circle with a bin angle $\frac{2\pi}{N_{bin}}$, d_i is the distance of the tumor cell farthest from the tumor center in the i -th bin, and $\langle d \rangle$ is average over the d_i , $\langle d \rangle = N_{bin}^{-1} \sum_{i=1}^{N_{bin}} d_i$. For our calculations, the bin number was set to $N_{bin} = 36$. The time evolution of gyradius and roughness as well as the growth curves for this set of experiments are presented in Figures 10, 11, and 12, respectively.

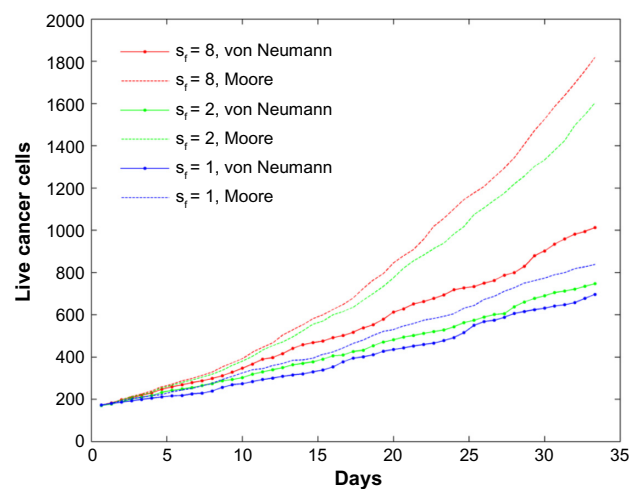


Figure 12. Tumor growth curves over time. Blue, green, and red lines denote the $s_f = 1, 2,$ and 8 cases, respectively. The von Neumann cases are plotted with dotted lines and the Moore with dashed lines.



It can be deduced that the importance of neighborhood selection is more evident as the distribution of the ECM becomes more rugged (top image of Fig. 8). As we have already mentioned, during the cellular migration process, a cell can only move to a neighborhood site that is empty. It is important to point out that the Moore neighborhood has twice the number of possible sites where a cell can move to comparing to the von Neumann neighborhood. When the ECM becomes harsh, this difference seems to play a significant role in tumor expansion allowing tumor cells to better sense and exploit their microenvironment and thus follow the free pathways around them.

It is evident that the Moore neighborhood relative to the von Neumann neighborhood, results in (i) faster tumor expansion as reflected in the time evolution of gyradius, (ii) increased morphological asymmetry in terms of tumor roughness, and (iii) increased viable tumor population as indicated by the growth curves.

Further experiments (results in Section 2 of Supplementary Material) also show that the differences in tumor growth and morphology between the two neighborhood schemes are enhanced under conditions that seem to promote invasion such as increased haptotactic coefficient and ECM degradation. However, it should be noted that an extensive investigation of the conditions under which the differences are more/less evident is important in order to examine more complex microenvironments and tumor cell responses. Also, the validation of the outcomes with real biological experiments is necessary for confirming these observations.

Statistical study of haptotactic movement. In order to verify the robustness of our outcomes as far as haptotaxis is concerned, N different random ECM distributions were produced. The experiments were then repeated with the same set of parameters for both neighborhood schemes. Specifically, $N = 100$ experiments were conducted for each neighborhood scheme, while the values of the haptotaxis coefficient (χ) and the cellular proliferation time (A_p) were $\chi = 4 \cdot 10^{-8} \text{ cm}^2 \text{ s}^{-1} \text{ M}^{-1}$ and $A_p = 16$ hours, respectively. The tumor morphology over time of the first set of experiments can be seen in the Supplementary haptotaxis videos. The experiments ran for 40 iterations (640 fictitious hours) and the time evolution of the gyradius, roughness, and the viable cell populations were estimated as shown in Figures 13, 14, and 15 correspondingly.

To test if the results had a statistical significance, we followed the same procedure as we did with the chemotaxis results. We initially used the D'Agostino–Pearson's K^2 test to verify whether our results from each population/iteration come from a normally distributed population. Then we performed coupled t -tests for unequal variances for all the time points between the von Neumann and the Moore set of experiments without using a multiple comparison adjustment method. For all the metrics, the differences were statistically important after a number of iterations. The p -values produced in the final time points were less

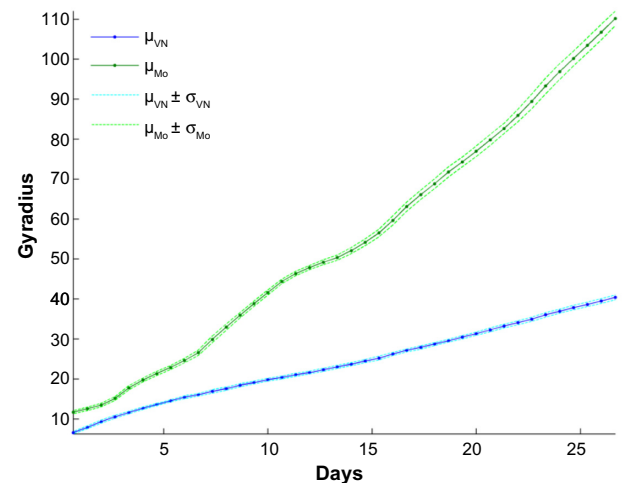


Figure 13. Mean values of gyradius over time. Dotted blue and green lines represent the mean populations for von Neumann and Moore, respectively. The ranges created by the blue and green pairs of dashed lines contain the mean values of the populations plus and minus their standard deviations.

than 10^{-9} for all the metrics (the gyradius, roughness, and population size).

In consistence with real tumor experiments that support linear growth of tumor diameter over time,^{31,32} the mean gyradius of the von Neumann–and the Moore–based tumors both grow linearly with a slope of 0.81 and 2.52, respectively. The difference in slopes indicates that the Moore-based tumors exhibit greater expansion rate. In addition, the tumor roughness is increased for the Moore-driven tumors, which implies higher invasion than the von Neumann–driven tumors.

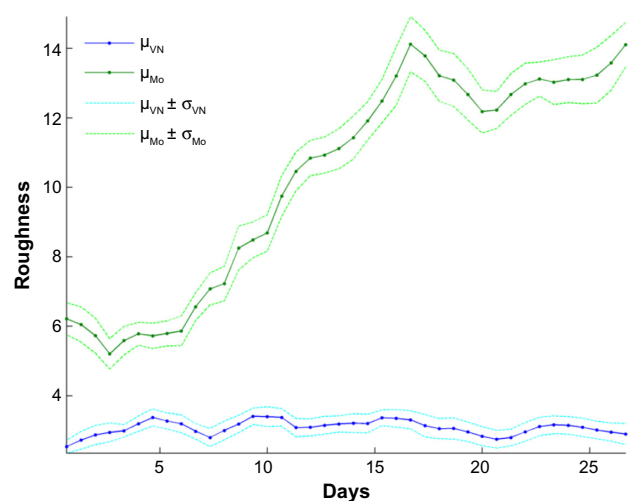


Figure 14. Mean values of roughness over time. Dotted blue and green lines represent the mean populations for von Neumann and Moore, respectively. The ranges created by the blue and green pairs of dashed lines contain the mean values of the populations plus and minus their standard deviations.

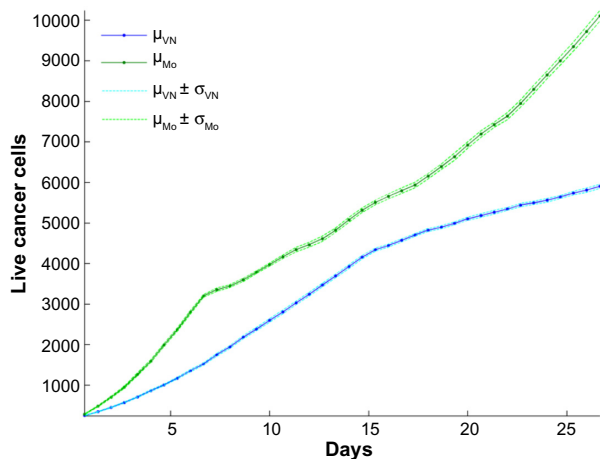


Figure 15. Mean values of cancer populations over time. Dotted blue and green lines represent the mean populations for von Neumann and Moore, respectively. The ranges created by the blue and green pairs of dashed lines contain the mean values of the populations plus and minus their standard deviations.

It should be noted that contrary to the von Neumann neighbor, the Moore neighbor predicts an initial slower expansion rate followed by a more rapid radial expansion.

Furthermore, the mean values of the viable tumor cell populations show that the cells following the von Neumann scheme result in reduced populations when compared to their Moore counterparts. What is more, the populations appear to switch to lower growth rates than the one they begin with. However, the growth deceleration takes place at different time points per case, 10th and 23rd iteration for the Moore and the von Neumann, respectively. At these particular time points, the growth slows down because oxygen levels fall below the viable threshold and necrotic cells appear. One would expect that the compact morphology would cause the center of the tumor to run out of oxygen faster than the invasive morphology, which could allow the oxygen to diffuse further to the core between the tendrils. However, necrotic cells appear earlier in the aggressive morphology than in the compact. This can be explained if we account for the tumor cells in quiescent state, which, as discussed in section 2, have halved their oxygen consumption. If we sum the mean values for the proliferative populations and the half of the quiescent populations

$\left(p_a + \frac{p_q}{2} \right)$, we get a measure of the total tumor oxygen consumption rate. Calculating that number at the aforementioned switching points, we get for both neighborhoods that the total consumption is approximately 3600γ . Thus, we can see that not only the number of cells but also the cell state is consequential as well.

Combining the knowledge from the gyration and roughness, it can be deduced that the major differences in the growth curves and morphologies can be attributed to the fact that the von Neumann-based tumors tend to grow in a condensed manner, which results in a tumor with many cells in

quiescent state, while the Moore-based tumors tend to expand more easily adopting a tendril-like morphology with substantially less quiescent cells.

Conclusion

The emergence of the invasive behavior throughout tumor evolution is highly associated with a fatal outcome. For this reason, the invasive phase of tumor growth has been the focus of numerous studies in an effort to understand its underlying mechanisms and predict its emergence and characteristic patterns as tumor evolves destroying the surrounding host tissue microenvironment. Early prognosis and accurate predictions are of high significance in clinical practice and aid in the application of early and effective treatments.

In this work, a hybrid model for tumor invasion has been adopted¹ by combining a continuum description of the variables that comprise the tumor microenvironment with a rule-based stochastic cellular automata model of the cellular behavior on a 2D square lattice. An expansion of a cell movement mechanism was introduced, enabling the cells to move from von Neumann neighborhood to Moore neighborhood essentially doubling the possible locations to which a cell can move. Then, the impact of the neighborhood scheme selection in tumor cell movement, growth, and morphology was studied.

We first performed 100 sets of experiments within a chemotactic context where we assumed that cellular movement was directed by the gradients of oxygen distribution. Although a homogeneously vascularized tumor is assumed, as the tumor grows in size, the oxygen supply becomes inadequate for the increased metabolic demands of tumor cells, allowing areas of differentiated oxygenation to form within the tumor mass. Due to the radial symmetry of the problem, a tumor of circular shape is expected. With that in mind, in order to assess the distance between our results and the valid circular morphology, we adopted a simple radial variance measure. The results showed that utilizing the Moore neighborhood, the method yields simulations closer to the expected circular morphology. Thus, the inclusion of the diagonal points improved the resulting morphology, alleviating the computational artifacts presented by the previous von Neumann-based approach. Additionally, we showed that the neighborhood choice introduces statistically important differences in the cancer cells population.

Furthermore, haptotaxis has also been explored. The work of Anderson et al.⁹ has shown that even when tumors comprise heterogeneous subpopulations when the ECM distribution is assumed homogeneous, a symmetric tumor is formed, whereas a random distribution of the ECM might be more realistic and allows the formation of invasive tumor morphologies similar to those observed in real tumors. Therefore, concentrations representing ECMs were initialized with random distributions, which were smoothed at a varying homogeneity degree. The Moore-based movement resulted in



tumor cells with a tendency to follow the ECM paths much easier, thus expanding faster and forming tumor patterns that highly differ from the corresponding von Neumann-based ones, which are considerably more compact. Furthermore, the simulations also show that as the ECM distribution becomes less smooth, the difference between the two neighborhood schemes becomes more evident. To quantify these different tendencies, we used the gyradius and the roughness metrics. All in all, should the environment allow it, the cells equipped with the expanded Moore neighborhood tumor cells are more prone to invasiveness. Finally, the robustness of our outcomes for the random extracellular cases was verified. We performed 100 experiments for each neighborhood with varying ECM distributions but kept a stable smoothing factor. The evaluated gyradius, roughness, and cell populations of all the experiments were submitted to a *t*-test, which showed that the deviations manifested by the neighborhood choice affected all three of these aspects and they were statistically important.

As cellular migration is critical for tumor growth and invasion, it stresses the importance to describe movement as adequately as possible. Cellular automata models on a regular lattice remain very popular due to their simplicity and direct relation with the continuum approaches, if the latter are solved using the finite-differences schema. Although lattice anisotropies arising from regular lattices can be circumvented by using random and isotropic lattices,^{14,30} as well as by using off-lattice models,¹² we demonstrate in this work how a simple extension from von Neumann to Moore neighborhood in cell migration on a regular lattice can better approximate cellular motility by minimizing the artifacts arising from lattice anisotropies and how the neighborhood selection can significantly affect tumor growth and morphology. Our study also shows that the importance of neighborhood selection can be more evident under specific conditions such as increased haptotaxis/chemotactic coefficient, harsher ECM distribution, and ECM degradation. An extensive exploration of various microenvironments and tumor behaviors with increasing complexity is required in order to better approximate real tumor patterns and reveal the conditions under which the differences between the movement approaches can become more/less evident. To this end, as real clinical cellular-level data of invasive tumors are hard to find and are difficult to control, *in vitro* experiments seem more promising for the validation of computational outcomes not least because they allow a better control of the involving components.³³

Acknowledgment

The numerical solution of the continuous compartment was developed by Georgios Grekas.

Author Contributions

All authors contributed to this work. Original idea and conception: GT, VS. Design of the experiments: ET, GT. Writing of the manuscript: GT, ET, VS. Structure and arguments for

the paper: GT, ET, VS. Critical revisions and approved final version: VS, KM.

Supplementary Materials

The importance of neighborhood scheme selection in agent-based tumor growth modeling—Sup.pdf

chemotaxis sample VN.avi

chemotaxis sample Mo.avi

haptotaxis sample VN.avi

haptotaxis sample Mo.avi

REFERENCES

1. Anderson ARA. A hybrid mathematical model of solid tumour invasion: the importance of cell adhesion. *Math Med Biol.* 2005;22:163–86.
2. Zaman MH, Trapani LM, Sieminski AL, et al. Migration of tumor cells in 3D matrices is governed by matrix stiffness along with cell-matrix adhesion and proteolysis. *Proc Natl Acad Sci U S A.* 2006;103(29):10889–94.
3. Friedl P, Alexander S. Cancer invasion and the microenvironment: plasticity and reciprocity. *Cell.* 2011;147(5):992–1009.
4. Pathak A, Kumar S. Independent regulation of tumor cell migration by matrix stiffness and confinement. *Proc Natl Acad Sci U S A.* 2012;109(26):10334–9.
5. Baker EL, Srivastava J, Yu D, Bonnecaze RT, Zaman MH. Cancer cell migration: integrated roles of matrix mechanics and transforming potential. *PLoS One.* 2011;6(5):e20355.
6. Carey SP, Rahman A, Kraning-Rush CM, et al. Comparative mechanisms of cancer cell migration through 3D matrix and physiological microtracks. *Am J Physiol Cell Physiol.* 2015;308(6):C436–47.
7. Kapoor A. Extracellular matrix density regulates extracellular proteolysis via modulation of cellular contractility. *J Carcinog Mutagen.* 2013;S13:003.
8. Kansal AR, Torquato S, Harsh GR IV, Chiocia EA, Deisboeck TS. Simulated brain tumor growth dynamics using a three-dimensional cellular automaton. *J Theor Biol.* 2000;203(4):367–82.
9. Anderson ARA, Weaver AM, Cummings PT, Quaranta V. Tumor morphology and phenotypic evolution driven by selective pressure from the microenvironment. *Cell.* 2006;127:905–15.
10. Fedotov S, Iomin A. Migration and proliferation dichotomy in tumor-cell invasion. *Phys Rev Lett.* 2007;98(11):118101.
11. Basanta D, Hatzikirou H, Deutsch A. Studying the emergence of invasiveness in tumours using game theory. *Eur Phys J B.* 2008;63(3):393–7.
12. Jeon J, Quaranta V, Cummings PT. An off-lattice hybrid discrete-continuum model of tumor growth and invasion. *Biophys J.* 2010;98(1):37–47.
13. Frieboes HB, Jin F, Chuang YL, Wise SM, Lowengrub JS, Cristini VV. Three-dimensional multispecies nonlinear tumor growth-II: tumor invasion and angiogenesis. *J Theor Biol.* 2010;264(4):1254–78.
14. Jiao Y, Torquato S. Emergent behaviors from a cellular automaton model for invasive tumor growth in heterogeneous microenvironments. *PLoS Comput Biol.* 2011;7(12):10–2.
15. Chaplain MAJ, Lachowicz M, Szymanska Z, Wrzosek D. Mathematical modeling of cancer invasion: the importance of cell-cell adhesion and cell-matrix adhesion. *Math Model Methods Appl Sci.* 2011;21(04):719–743.
16. Tektonidis M, Hatzikirou H, Chauvière A, Simon M, Schaller K, Deutsch A. Identification of intrinsic *in vitro* cellular mechanisms for glioma invasion. *J Theor Biol.* 2011;287:131–47.
17. Tzamali E, Grekas G, Marias K, Sakkalis V. Exploring the competition between proliferative and invasive cancer phenotypes in a continuous spatial model. *PLoS One.* 2014;9(8):e103191.
18. Bertaux F, Stoma S, Drasdo D, Batt G. Modeling dynamics of cell-to-cell variability in TRAIL-induced apoptosis explains fractional killing and predicts reversible resistance. *PLoS Comput Biol.* 2014;10(10):e1003893.
19. Ramis-Conde I, Chaplain MAJ, Anderson ARA. Mathematical modelling of cancer cell invasion of tissue. *Math Comput Model.* 2008;47(5–6):533–45.
20. Swanson KR, Rockne RC, Claridge J, Chaplain MA, Alvord EC, Anderson ARA. Quantifying the role of angiogenesis in malignant progression of gliomas: *in silico* modeling integrates imaging and histology. *Cancer Res.* 2011;71:7366–75.
21. Wise SM, Lowengrub JS, Frieboes HB, Cristini V. Three-dimensional multispecies nonlinear tumor growth-I. Model and numerical method. *J Theor Biol.* 2008;253:524–43.
22. Rejniak KA, Anderson ARA. Hybrid models of tumor growth. *Wiley Interdiscip Rev Syst Biol Med.* 2011;3:115–25.



23. Gerlee P, Kim E, Anderson ARA. Bridging scales in cancer progression: mapping genotype to phenotype using neural networks. *Semin Cancer Biol.* 2015;30:30–41.
24. Codling EA, Plank MJ, Benhamou S. Random walk models in biology. *J R Soc Interface.* 2008;5:813–34.
25. Anderson AR, Chaplain MA. Continuous and discrete mathematical models of tumor-induced angiogenesis. *Bull Math Biol.* 1998;60(5):857–99.
26. Chen J-B. A generalized optimal 9-point scheme for frequency-domain scalar wave equation. *J Appl Geophys.* 2013;92:1–7.
27. Jo CH, Shin C, Suh JH. An optimal 9-point, finite-difference, frequency-space, 2-D scalar wave extrapolator. *Geophysics.* 1996;61(2):529–37.
28. Deisboeck TS, Berens ME, Kansal AR, Torquato S, Stemmer-Rachamimov AO, Chiocca EA. Pattern of self-organization in tumour systems: complex growth dynamics in a novel brain tumour spheroid model. *Cell Prolif.* 2001;34(2): 115–34.
29. Tzedakis G, Grekas G, Tzamali E, Marias K, Sakkalis V. The importance of grid size and boundary conditions in discrete tumor growth modeling. In *Silico Oncology and Cancer Investigation (IARWISOCI), 2014 6th International Advanced Research Workshop on.* Nov 2014;1(4):3–4.
30. Drasdo D. Coarse graining in simulated cell populations. *Adv Complex Syst.* 2005;08:319–63.
31. Brú A, Pastor JM, Fernaud I, Brú I, Melle S, Berenguer C. Super-rough dynamics on tumor growth. *Phys Rev Lett.* 1998;81(18):4008–11.
32. Swanson KR, Harpold HL, Peacock DL, et al. Velocity of radial expansion of contrast-enhancing gliomas and the effectiveness of radiotherapy in individual patients: a proof of principle. *Clin Oncol (R Coll Radiol).* 2008;20(4):301–8.
33. Kam Y, Rejniak KA, Anderson ARA. Cellular modeling of cancer invasion: integration of in silico and in vitro approaches. *J Cell Physiol.* 2012;227:431–8.